Forceful Aerial Manipulation based on an Aerial Robotic Chain: Hybrid Modeling and Control

Huan Nguyen[1], and Kostas Alexis[2]

***Abstract*—This paper presents the system design, modeling, and control of the Aerial Robotic Chain Manipulator. This new robot design offers the potential to exert strong forces and moments on the environment, carry and lift significant payloads, and simultaneously navigate through narrow corridors. We contribute a hybrid modeling framework to model the system both in Free-flight mode, where the end-effector acts as a normal pendulum, and in Aerial Manipulation mode, where the system behaves as an inverted pendulum. Respective controllers are designed for both operating modes with stability guarantees provided by Lyapunov theory. The presented experimental studies include a task of valve rotation, a pick-and-release task, and the verification of load oscillation suppression to demonstrate the stability and performance of the system.**

***Index Terms*—Aerial systems: mechanics and control, multi-robot systems, aerial robot manipulation**

I. INTRODUCTION

RESEARCH in aerial robotics is pushing the frontier of autonomy, sensing, processing and endurance of Micro Aerial Vehicles (MAVs). Flying robots are being integrated in an ever increasing set of applications such as inspection, surveillance, or even physical interaction and manipulation [1–4]. However, aerial robots still present a set of key limitations. Largely, existing MAV designs are monolithic and thus present a common set of trade-offs, for example between payload and endurance or size. In the domain of aerial manipulation this implies rather sensitive designs with limited work-task execution capacity or resorting to large, complex and expensive platforms. Responding to a subset of these needs, reconfigurable and multilinked systems-of-systems of aerial robots have emerged [5–11] including our recent contribution on the Aerial Robotic Chain (ARC) [12]. Multilinked aerial systems such as the ARC can exploit a different design space and achieve simultaneously the ability to cross narrow sections, ferry significant payloads, enable distributed sensing and processing, incorporate redundancy and more. In this work we extend the potential of ARC by developing a custom aerial manipulation solution and proposing the modeling framework and control strategy that allow forceful physical interaction for work-task execution. The proposed design extension of the aerial robotic chain, called "Aerial Robotic Chain Manipulator" (ARC-M) is a multilinked robot consisting of two quadrotors (ARC-units) connected, using 3-Degree of Freedom (DoF) joints, through a rigid link that incorporates a manipulator with a lightweight finger end-effector. Fig. 1 depicts the system. Through its design, ARC-M presents a set of capabilities, including the ability to a) exert strong forces and moments, b) carry and lift significant payloads, and c) navigate narrow cross sections. Contrary to the majority of aerial manipulator designs where a single aerial robot is the basis for the overall force and moment exertion, ARC-M can apply significantly stronger moments and forces due to its ability to use the thrust vectoring of two independent quadrotors that are connected at a distance to each other and from the end-effector.

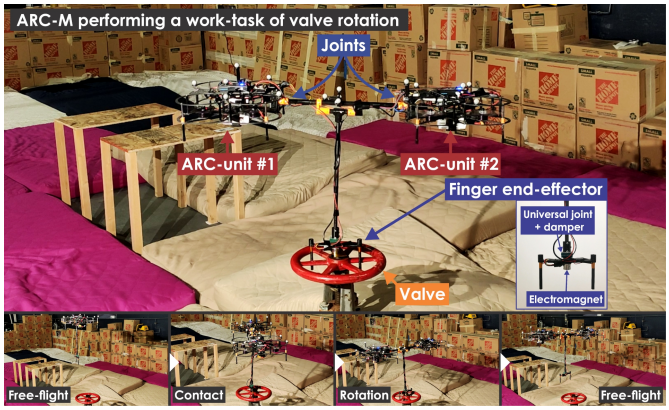

Fig. 1. The Aerial Robotic Chain Manipulator (ARC-M) performing a work-task involving forceful valve rotation.

Beyond the design of ARC-M, this paper further contributes a) a hybrid modeling framework capturing both the free-flight and aerial manipulation modes of this multilinked aerial robot, as well as b) the control strategy for autonomous navigation and forcible aerial manipulation. In free-flight the end-effector behaves as a normal pendulum, whereas during aerial manipulation the whole system acts analogously to an inverted pendulum. The control design is accompanied with stability proof for both modes. The controller performance and its stability are demonstrated through a set of experimental studies relating to challenging work-task execution. Those include a) valve rotation and b) pick-and-release of objects, alongside c) verification of payload transfer stability.

Regarding the remainder of this paper: Section II presents related work. Section III overviews the system. Modeling and control are presented in Sections IV, and V, followed by results in Section VI and conclusions in Section VII.

Manuscript received: October, 15, 2020; Revised January, 11, 2021; Accepted February, 16, 2021. This paper was recommended for publication by Editor Pauline Pounds upon evaluation of the Associate Editor and Reviewers' comments. This work was supported by the NSF IIS Core Award "RI: Small: Learning Resilient Autonomous Flight Behaviors by Exploiting Collision-tolerance" under award No. 2008904.

[1]Huan Nguyen is with the Autonomous Robots Lab, Department of Engineering Cybernetics, Norwegian University of Science and Technology, 7491 Trondheim, Norway (email: dinh.h.nguyen@ntnu.no)

[2]Kostas Alexis is with the Autonomous Robots Lab, University of Nevada, Reno, 1664 N. Virginia, 89557, Reno, NV, USA (email: kalexis@unr.edu)

Digital Object Identifier (DOI): see top of this page.

II. RELATED WORK

This work relates to two sets of research studies, namely in the domains of a) multilinked aerial robots, and b) aerial manipulation. With respect to the first, the DRAGON robotic system [5, 6] is one of the most notable examples and is a dual-rotor-embedded multilink system with the ability of multi-DoF transformation. It can control the full pose in $\mathcal{SE}(3)$ and through a prototype consisting of four links, it demonstrates the ability to adjust its shape to go through a narrow window. The Large-Size Aerial Skeleton with Distributed Rotor Actuation (LASDRA) [7] is a system that integrates distributed rotor 6DoF full actuation of each link. Its rotors are backdrivable and it relies on distributed impedance control. The work in [8, 9] presents a multilinked multirotor made to enable the transportation of objects of significant size by exploiting form adaptation.

In the domain of aerial manipulation and broadly physical interaction, a set of approaches have been proposed. A set of researchers have contributed in the domain of physical interaction [13, 14], while the area has developed to cover complicated aerial manipulation [3, 4]. In this area, diverse manipulator designs have been proposed - from arms [2, 15], to delta configurations [16], multi-robot manipulation [17] and more - alongside a set of control strategies [18–21]. A common characteristic of these contributions is that the ability to exert significant forces and moments has to rely on the size and thrust generation capabilities of a typically underactuated aerial robot and thus often severe limitations apply. A different approach is presented in [10, 11] through multiple quadrotors connected to a rigid frame. This work contributes ARC-M and intersects the domains of multilinked multi-robot aerial robots and aerial manipulation.

III. SYSTEM OVERVIEW

ARC-M extends the ARC-Alpha robot [12], with the addition of the finger end-effector connected to the link through a lightweight carbon tube. The end-effector is equipped with an electromagnet to be able to attach to or pickup metallic objects. The manipulator carbon fiber tube is connected to the finger through a universal joint incorporating a stiff damper (Fig. 1) thus the finger has approximately the same orientation as the link in Free-flight mode and also acts as a compliant mechanism when attached to a fixed point in Aerial Manipulation mode. The length of the link connecting the 2 ARC-units is 0.37m and the length of the carbon tube to the finger is 0.42m. The masses of the finger, link and each ARC-unit are 90g, 150g and 900g, respectively.

IV. MODELING

In order to develop a model for the ARC-M system we first acknowledge the fact that the process of transition from free-flight to physical interaction takes place in infinitesimal time as the collision-dynamics are extremely fast. Given this observation, the dynamics of the system are modeled as a hybrid dynamical model with two modes of the Aerial Robotic Chain $\mathbf{Q} = (FF, AM)$, namely a) Free-Flight (FF) and b) Aerial Manipulation (AM). We use the framework of hybrid automata [22] to model this hybrid system as visualized in Fig. 2. The Domain Maps and Flow Maps governing the system in each mode are presented in Sections IV-A and IV-B, while the Guard Maps describing switching conditions between the modes and the Reset Maps encoding the state of the system after the switch are described in Section IV-C. The above hybrid system is simulated using the Hybrid Systems Simulation Toolbox for Matlab/Simulink (HyEQ) [23]. The notations used are defined in Table I and Fig. 3.

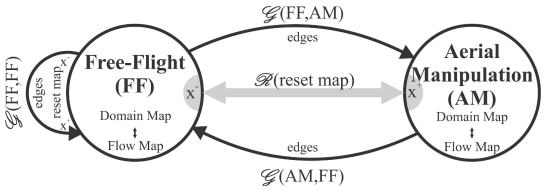

Fig. 2. Hybrid modeling diagram for the ARC-M system.

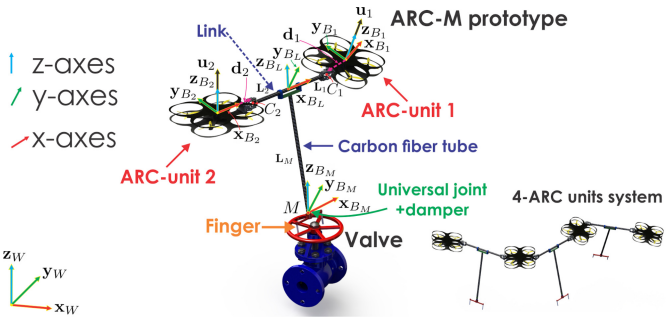

Fig. 3. Visualization of the system and coordinate frames. In this CAD model the ARC-M is depicted in the context of a valve-turning task.

The origin C_L of $\mathbb{B}_L$ is chosen as a point on the link such that $m_1\mathbf{L}_1 + m_2\mathbf{L}_2 = \mathbf{0}$. From the design of ARC-M, it holds that $\mathbf{L} = L\mathbf{e}_1, \mathbf{L}_M = -L_M\mathbf{e}_3$. We utilize the attitude error function Ψ on $\mathcal{SO}(3)$, the attitude error vector $\mathbf{e}_R$ and the angular velocity error vector $\mathbf{e}_\Omega$ defined in [24]:

$$\Psi(\mathbf{R}_1, \mathbf{R}_2) = \frac{1}{2}\,\mathrm{tr}\left(\mathbf{I} - \mathbf{R}_2^T\mathbf{R}_1\right) \tag{1}$$

$$\mathbf{e}_R(\mathbf{R}_1, \mathbf{R}_2) = \frac{1}{2}(\mathbf{R}_2^T\mathbf{R}_1 - \mathbf{R}_1^T\mathbf{R}_2)^\vee \tag{2}$$

$$\mathbf{e}_\Omega(\mathbf{\Omega}_1, \mathbf{\Omega}_2) = \mathbf{\Omega}_1 - \mathbf{R}_1^T\mathbf{R}_2\mathbf{\Omega}_2 \tag{3}$$

The friction and twist moments that the damper and the universal joint apply to the finger and the carbon fiber tube are derived in [25] and given as:

$$\mathbf{M}^L_{fric} = -\mathbf{R}_L^T\mathbf{b}_M\mathbf{R}_L\mathbf{e}_\Omega(\mathbf{\Omega}_L, \mathbf{\Omega}_M) \tag{4}$$

$$\mathbf{M}^M_{fric} = -\mathbf{R}_M^T\mathbf{b}_M\mathbf{R}_M\mathbf{e}_\Omega(\mathbf{\Omega}_M, \mathbf{\Omega}_L) \tag{5}$$

$$\mathbf{M}^L_{twist} = \frac{1}{4}\left[\mathrm{tr}(\mathbf{R}_L^T\mathbf{R}_M)\mathbf{I} - \mathbf{R}_M^T\mathbf{R}_L\right]\mathbf{k}_M(\mathbf{R}_L^T\mathbf{R}_M - \mathbf{R}_M^T\mathbf{R}_L)^\vee \tag{6}$$

$$\mathbf{M}^M_{twist} = -\frac{1}{4}\left[\mathrm{tr}(\mathbf{R}_M^T\mathbf{R}_L)\mathbf{I} - \mathbf{R}_L^T\mathbf{R}_M\right]\mathbf{k}_M(\mathbf{R}_L^T\mathbf{R}_M - \mathbf{R}_M^T\mathbf{R}_L)^\vee \tag{7}$$

A. Free-flight Dynamics

When the robot operates in the Free-flight mode, the link can freely rotate around the two 3-DoF joints at C_1 and C_2, therefore the finger is considered as a normal pendulum. The state of the ARC-M multi-body system in this mode is:

$$\mathbf{x}_{FF} = [\mathbf{x}_L, \mathbf{v}_L, \mathbf{R}_1, \mathbf{\Omega}_1, \mathbf{R}_2, \mathbf{\Omega}_2, \mathbf{R}_L, \mathbf{\Omega}_L, \mathbf{R}_M, \mathbf{\Omega}_M]^T$$

with domain map:

TABLE I
NOTATIONS USED IN THE PAPER

$\mathbb{W}, \mathbb{B}_L, \mathbb{B}_M, \mathbb{B}_i$	World frame, body-fixed frame of the link, finger and ARC-unit i $(i = 1, 2)$ frames
$\{\mathbf{e}_1, \mathbf{e}_2, \mathbf{e}_3\}$	Unit-vectors in x, y, z axes
$m_L, m_M, m_i \in \mathbb{R}$	Link, finger, ARC-units i $(i = 1, 2)$'s mass
C_L, M, C_i	Origins of $\mathbb{B}_L, \mathbb{B}_M$ and the joint connecting the link to ARC-unit i $(i = 1, 2)$
$L, L_M \in \mathbb{R}$	Length of the link connecting 2 ARC-units, the carbon tube connecting C_L to the finger
$\mathbf{L}, \mathbf{L}_M, \mathbf{L}_i \in \mathbb{R}^3$	Vectors $\overrightarrow{C_2C_1}, \overrightarrow{C_LM}, \overrightarrow{C_LC_i}$ $(i = 1, 2)$ expressed in $\mathbb{B}_L$
$\mathbf{d}_i \in \mathbb{R}^3$	Vector from the Center-of-Gravity (CoG) of ARC-unit i to the joint C_i, expressed in $\mathbb{B}_i$ $(i = 1, 2)$
$\mathbf{u}_i \in \mathbb{R}^3$	Thrust vector generated by ARC-unit i $(i = 1, 2)$, expressed in $\mathbb{W}$
$\mathbf{M}_i \in \mathbb{R}^3$	Moment generated by ARC-unit i, expressed in $\mathbb{B}_i$ $(i = 1, 2)$
$\mathbf{x}_L, \mathbf{x}_M, \mathbf{x}_i \in \mathbb{R}^3$	Positions of C_L, the finger and ARC-unit i $(i = 1, 2)$ expressed in $\mathbb{W}$
(x_L, y_L, z_L)	x,y,z coordinates of $\mathbf{x}_L$
$\mathbf{v}_L, \mathbf{v}_M, \mathbf{v}_i \in \mathbb{R}^3$	Velocities of C_L, the finger and ARC-unit i $(i = 1, 2)$ expressed in $\mathbb{W}$
$\mathbf{R}_L, \mathbf{R}_M, \mathbf{R}_i \in \mathcal{SO}(3)$	Rotation matrices from $\mathbb{B}_L, \mathbb{B}_M, \mathbb{B}_i$ $(i = 1, 2)$ to $\mathbb{W}$
$(\phi_L, \theta_L, \psi_L)$	Roll, pitch, yaw Euler angles of the link
$\mathbf{\Omega}_L, \mathbf{\Omega}_M, \mathbf{\Omega}_i \in \mathbb{R}^3$	Angular velocities of the link expressed in $\mathbb{B}_L$, finger in $\mathbb{B}_M$, ARC-unit i in $\mathbb{B}_i$, $(i = 1, 2)$
$\mathbf{J}_L, \mathbf{J}_M, \mathbf{J}_i \in \mathbb{S}^3_{++}$	Inertia matrices of the link expressed in $\mathbb{B}_L$, finger in $\mathbb{B}_M$, ARC-unit i in $\mathbb{B}_i$ $(i = 1, 2)$
$\mathbf{J}_{MC} \in \mathbb{S}^3_{++}$	Lumped inertia matrix of finger and valve expressed in $\mathbb{B}_M (\mathbf{J}_{MC} = \mathbf{J}_M + \mathbf{J}_{valve})$
$\mathbf{k}_M, \mathbf{b}_M \in \mathbb{S}^3_{++}$	Stiffness and friction coefficient matrices of the damper between finger and link, the effect of the universal joint is also accounted
$\mathbf{M}^L_{fric}, \mathbf{M}^M_{fric} \in \mathbb{R}^3$	Friction moments that the damper and the universal joint apply to the carbon fiber tube expressed in $\mathbb{B}_L$, the finger expressed in $\mathbb{B}_M$
$\mathbf{M}^L_{twist}, \mathbf{M}^M_{twist} \in \mathbb{R}^3$	Twist moments that the damper and the universal joint apply to the carbon fiber tube expressed in $\mathbb{B}_L$, the finger expressed in $\mathbb{B}_M$
$\mathbf{M}^V_{fric} \in \mathbb{R}^3$	Moment by friction force applied to the valve when moving expressed in $\mathbb{B}_M$ $(\mathbf{M}^V_{fric} \parallel \mathbf{e}_3)$
$\mathbf{M}^V_{ext} \in \mathbb{R}^3$	Other moments applied by valve's base to the valve compensating for the moments in xy directions that the damper applies to the finger in AM mode expressed in $\mathbb{B}_M$ $(\mathbf{M}^V_{ext} \perp \mathbf{e}_3)$
$\mathbf{F}^{mag}$	Holding force of the electromagnet expressed in $\mathbb{B}_M$, $\mathbf{F}^{mag} = 0$ when it is turned off
$\mathbf{x}^d$	$\mathbf{x}$ Reference value (scalar, vector or matrix)
$\hat{\mathbf{x}} \in \mathbb{R}^{3\times3}, \mathbf{A}^\vee \in \mathbb{R}^3$	hat operator and its inverse, vee operator
$\mathbf{x} \cdot \mathbf{y}$	dot product of 2 vectors $\mathbf{x}$ and $\mathbf{y}$
$(\mathbf{a}_x, \mathbf{a}_y, \mathbf{a}_z)$	Projected components of vector $\mathbf{a}$ in x, y, z axes of the frame that $\mathbf{a}$ is expressed in
$\mathrm{tr}(\mathbf{A}), \|\mathbf{A}\|_2$	Trace and 2-norm of matrix $\mathbf{A}$
$\lambda_m(\mathbf{A}), \lambda_M(\mathbf{A})$	Smallest and largest eigenvalues of matrix $\mathbf{A}$

$$\mathscr{D}(FF) = \mathbb{R}^3 \times \mathbb{R}^3 \times \mathcal{SO}(3) \times \mathbb{R}^3 \times \mathcal{SO}(3) \times \mathbb{R}^3 \times \mathcal{SO}(3) \times \mathbb{R}^3 \times \mathcal{SO}(3) \times \mathbb{R}^3 \tag{8}$$

Applying the extended Hamilton's principle with variations on the configuration manifold as in [26], we obtain the dynamics equations describing the system in Free-flight:

$$\begin{aligned} m_\Sigma \ddot{\mathbf{x}}_L + m_1\mathbf{R}_1\hat{\mathbf{d}}_1\dot{\mathbf{\Omega}}_1 + m_2\mathbf{R}_2\hat{\mathbf{d}}_2\dot{\mathbf{\Omega}}_2 - m_M\mathbf{R}_L\hat{\mathbf{L}}_M\dot{\mathbf{\Omega}}_L = \\ \mathbf{u}_1 + \mathbf{u}_2 - m_\Sigma g\mathbf{e}_3 + m_1\mathbf{R}_1\hat{\mathbf{\Omega}}_1^2\mathbf{d}_1 + m_2\mathbf{R}_2\hat{\mathbf{\Omega}}_2^2\mathbf{d}_2 - m_M\mathbf{R}_L\hat{\mathbf{\Omega}}_L^2\mathbf{L}_M \end{aligned} \tag{9}$$

$$\begin{aligned} -m_1\hat{\mathbf{d}}_1\mathbf{R}_1^T\ddot{\mathbf{x}}_L + (\mathbf{J}_1 - m_1\hat{\mathbf{d}}_1^2)\dot{\mathbf{\Omega}}_1 + m_1\hat{\mathbf{d}}_1\mathbf{R}_1^T\mathbf{R}_L\hat{\mathbf{L}}_1\dot{\mathbf{\Omega}}_L = \\ \mathbf{M}_1 - \hat{\mathbf{d}}_1\mathbf{R}_1^T\mathbf{u}_1 + m_1\hat{\mathbf{d}}_1\mathbf{R}_1^T\mathbf{R}_L\hat{\mathbf{\Omega}}_L^2\mathbf{L}_1 \\ - \hat{\mathbf{\Omega}}_1(\mathbf{J}_1 - m_1\hat{\mathbf{d}}_1^2)\mathbf{\Omega}_1 + m_1g\hat{\mathbf{d}}_1\mathbf{R}_1^T\mathbf{e}_3 \end{aligned} \tag{10}$$

$$\begin{aligned} -m_2\hat{\mathbf{d}}_2\mathbf{R}_2^T\ddot{\mathbf{x}}_L + (\mathbf{J}_2 - m_2\hat{\mathbf{d}}_2^2)\dot{\mathbf{\Omega}}_2 + m_2\hat{\mathbf{d}}_2\mathbf{R}_2^T\mathbf{R}_L\hat{\mathbf{L}}_2\dot{\mathbf{\Omega}}_L = \\ \mathbf{M}_2 - \hat{\mathbf{d}}_2\mathbf{R}_2^T\mathbf{u}_2 + m_2\hat{\mathbf{d}}_2\mathbf{R}_2^T\mathbf{R}_L\hat{\mathbf{\Omega}}_L^2\mathbf{L}_2 \\ - \hat{\mathbf{\Omega}}_2(\mathbf{J}_2 - m_2\hat{\mathbf{d}}_2^2)\mathbf{\Omega}_2 + m_2g\hat{\mathbf{d}}_2\mathbf{R}_2^T\mathbf{e}_3 \end{aligned} \tag{11}$$

$$\begin{aligned} m_M\hat{\mathbf{L}}_M\mathbf{R}_L^T\ddot{\mathbf{x}}_L + m_1\hat{\mathbf{L}}_1\mathbf{R}_L^T\mathbf{R}_1\hat{\mathbf{d}}_1\dot{\mathbf{\Omega}}_1 + m_2\hat{\mathbf{L}}_2\mathbf{R}_L^T\mathbf{R}_2\hat{\mathbf{d}}_2\dot{\mathbf{\Omega}}_2 \\ + \bar{\mathbf{J}}_{Lf}\dot{\mathbf{\Omega}}_L = \hat{\mathbf{L}}_1\mathbf{R}_L^T\mathbf{u}_1 + \hat{\mathbf{L}}_2\mathbf{R}_L^T\mathbf{u}_2 - \hat{\mathbf{\Omega}}_L\bar{\mathbf{J}}_{Lf}\mathbf{\Omega}_L - m_Mg\hat{\mathbf{L}}_M\mathbf{R}_L^T\mathbf{e}_3 \\ + m_1\hat{\mathbf{L}}_1\mathbf{R}_L^T\mathbf{R}_1\hat{\mathbf{\Omega}}_1^2\mathbf{d}_1 + m_2\hat{\mathbf{L}}_2\mathbf{R}_L^T\mathbf{R}_2\hat{\mathbf{\Omega}}_2^2\mathbf{d}_2 + \mathbf{M}^L_{fric} + \mathbf{M}^L_{twist} \end{aligned} \tag{12}$$

$$\mathbf{J}_M\dot{\mathbf{\Omega}}_M = -\hat{\mathbf{\Omega}}_M\mathbf{J}_M\mathbf{\Omega}_M + \mathbf{M}^M_{fric} + \mathbf{M}^M_{twist} \tag{13}$$

where $m_\Sigma = m_1 + m_2 + m_L + m_M$ and $\bar{\mathbf{J}}_{Lf} = \mathbf{J}_L - m_1\hat{\mathbf{L}}_1^2 - m_2\hat{\mathbf{L}}_2^2 - m_M\hat{\mathbf{L}}_M^2$.

From (9)-(13), we observe that the translational dynamics of the system, the rotational dynamics of the link, each ARC-unit and the finger are coupled with each other. Neglecting the terms related to the offset between the joint and the CoG of each ARC-unit $(\mathbf{d}_1, \mathbf{d}_2)$, (10), (11) become typical of the rotational dynamics of a single quadrotor. Equation (9) describes the translational dynamics of the link; given that $m_M \ll m_1 + m_2 + m_L$, the rotational dynamics of the link have little effect on its translation dynamics. However, as per (12) the rotational dynamics of the link are influenced by its translation through $\hat{\mathbf{L}}_M\mathbf{R}_L^T(-m_M\ddot{\mathbf{x}}_L)$, which is the moment of the inertial force experienced in $\mathbb{B}_L$. Equation (13) describes the rotational dynamics of the finger, where the last two terms illustrate the coupling between the rotational dynamics of the link and the end-effector.

B. Aerial Manipulation Dynamics

When in Aerial Manipulation mode, the finger of ARC-M is attached to the manipulating object - for example, a *valve*. In practice this is a stable connection as it is intended to manipulate primarily metallic objects and an electromagnet is also integrated on the finger. Given this consideration, $\mathbf{x}_M$ is fixed in $\mathbb{W}$. Thus, the link and the two ARC-units in this mode behave as an inverted pendulum. The state of the ARC-M multi-body system in Aerial Manipulation mode is:

$$\mathbf{x}_{AM} = [\mathbf{R}_1, \mathbf{\Omega}_1, \mathbf{R}_2, \mathbf{\Omega}_2, \mathbf{R}_L, \mathbf{\Omega}_L, \mathbf{R}_M, \mathbf{\Omega}_M]^T$$

with the domain map:

$$\mathscr{D}(AM) = \mathcal{SO}(3) \times \mathbb{R}^3 \times \mathcal{SO}(3) \times \mathbb{R}^3 \times \mathcal{SO}(3) \times \mathbb{R}^3 \times \mathcal{SO}(3) \times \mathbb{R}^3 \tag{14}$$

The dynamics equations describing the system are given as:

$$\begin{aligned} (\mathbf{J}_1 - m_1\hat{\mathbf{d}}_1^2)\dot{\mathbf{\Omega}}_1 + m_1\hat{\mathbf{d}}_1\mathbf{R}_1^T\mathbf{R}_L\hat{\mathbf{L}}_{M1}\dot{\mathbf{\Omega}}_L = \mathbf{M}_1 - \hat{\mathbf{d}}_1\mathbf{R}_1^T\mathbf{u}_1 \\ + m_1\hat{\mathbf{d}}_1\mathbf{R}_1^T\mathbf{R}_L\hat{\mathbf{\Omega}}_L^2\mathbf{L}_{M1} - \hat{\mathbf{\Omega}}_1(\mathbf{J}_1 - m_1\hat{\mathbf{d}}_1^2)\mathbf{\Omega}_1 + m_1g\hat{\mathbf{d}}_1\mathbf{R}_1^T\mathbf{e}_3 \end{aligned} \tag{15}$$

$$\begin{aligned} (\mathbf{J}_2 - m_2\hat{\mathbf{d}}_2^2)\dot{\mathbf{\Omega}}_2 + m_2\hat{\mathbf{d}}_2\mathbf{R}_2^T\mathbf{R}_L\hat{\mathbf{L}}_{M2}\dot{\mathbf{\Omega}}_L = \mathbf{M}_2 - \hat{\mathbf{d}}_2\mathbf{R}_2^T\mathbf{u}_2 \\ + m_2\hat{\mathbf{d}}_2\mathbf{R}_2^T\mathbf{R}_L\hat{\mathbf{\Omega}}_L^2\mathbf{L}_{M2} - \hat{\mathbf{\Omega}}_2(\mathbf{J}_2 - m_2\hat{\mathbf{d}}_2^2)\mathbf{\Omega}_2 + m_2g\hat{\mathbf{d}}_2\mathbf{R}_2^T\mathbf{e}_3 \end{aligned} \tag{16}$$

$$\begin{aligned} m_1\hat{\mathbf{L}}_{M1}\mathbf{R}_L^T\mathbf{R}_1\hat{\mathbf{d}}_1\dot{\mathbf{\Omega}}_1 + m_2\hat{\mathbf{L}}_{M2}\mathbf{R}_L^T\mathbf{R}_2\hat{\mathbf{d}}_2\dot{\mathbf{\Omega}}_2 + \mathbf{J}_{La}\dot{\mathbf{\Omega}}_L = \\ \hat{\mathbf{L}}_{M1}\mathbf{R}_L^T\mathbf{u}_1 + \hat{\mathbf{L}}_{M2}\mathbf{R}_L^T\mathbf{u}_2 - \hat{\mathbf{\Omega}}_L\mathbf{J}_{La}\mathbf{\Omega}_L + (m_1 + m_2 + m_L)g\hat{\mathbf{L}}_M\mathbf{R}_L^T\mathbf{e}_3 \\ + m_1\hat{\mathbf{L}}_{M1}\mathbf{R}_L^T\mathbf{R}_1\hat{\mathbf{\Omega}}_1^2\mathbf{d}_1 + m_2\hat{\mathbf{L}}_{M2}\mathbf{R}_L^T\mathbf{R}_2\hat{\mathbf{\Omega}}_2^2\mathbf{d}_2 + \mathbf{M}^L_{fric} + \mathbf{M}^L_{twist} \end{aligned} \tag{17}$$

$$\mathbf{J}_{MC}\dot{\mathbf{\Omega}}_M = -\hat{\mathbf{\Omega}}_M\mathbf{J}_{MC}\mathbf{\Omega}_M + \mathbf{M}^M_{fric} + \mathbf{M}^M_{twist} + \mathbf{M}^V_{fric} + \mathbf{M}^V_{ext} \tag{18}$$

where $\mathbf{L}_{Mi} = \mathbf{L}_i - \mathbf{L}_M$ $(i = 1, 2)$ and $\mathbf{J}_{La} = \mathbf{J}_L - m_1\hat{\mathbf{L}}_{M1}^2 - m_2\hat{\mathbf{L}}_{M2}^2 - m_L\hat{\mathbf{L}}_M^2$.

When neglecting terms containing $\mathbf{d}_1, \mathbf{d}_2$, (15), (16) describe the rotational dynamics of the 2 ARC-units. The rotational dynamics of the link and the finger are governed by (17), (18) and are coupled through the terms for the effects of the damper and universal joint.

C. Guards and Resets

The transition from the FF to AM mode only occurs when the finger's pose is close to the valve's pose, and the electromagnet is turned on. We derive the guard maps $\mathscr{G}$:

$$\begin{aligned}\mathscr{G}(FF, AM) = \{\mathbf{x}_{FF} |\ || \mathbf{x}_M - \mathbf{x}_{valve}||_2 \leqslant r_{th}, \\ \Psi(\mathbf{R}_M, \mathbf{R}_{valve}) \leqslant \Psi_{th}, ||\mathbf{F}^{mag}||_2 > 0\}\end{aligned} \tag{19}$$

$$\begin{aligned}\mathscr{G}(FF, FF) = \{\mathbf{x}_{FF} |\ ||\mathbf{x}_M - \mathbf{x}_{valve}||_2 > r_{th} \textbf{ or} \\ \Psi(\mathbf{R}_M, \mathbf{R}_{valve}) > \Psi_{th} \textbf{ or } ||\mathbf{F}^{mag}||_2 = 0\}\end{aligned} \tag{20}$$

where $\mathbf{x}_M = \mathbf{x}_L + \mathbf{R}_L\mathbf{L}_M, \mathbf{x}_{valve}$ is the contact point's position, Ψ is the attitude error function as in (1), r_{th},Ψ_{th} are positive thresholds. Transition from AM mode back to FF occurs when the electromagnet's holding force cannot keep the finger attached to the valve. Thus the guard map:

$$\begin{aligned}\mathscr{G}(AM, FF) = \{\mathbf{x}_{AM} |\ |(\mathbf{F}_M^{int} - m_M g\mathbf{e}_3)\cdot\mathbf{R}_M\mathbf{e}_1| > \mathbf{F}_x^{mag} \textbf{ or} \\ |(\mathbf{F}_M^{int} - m_M g\mathbf{e}_3)\cdot\mathbf{R}_M\mathbf{e}_2| > \mathbf{F}_y^{mag} \textbf{ or} \\ (\mathbf{F}_M^{int} - m_M g\mathbf{e}_3)\cdot\mathbf{R}_M\mathbf{e}_3 > \mathbf{F}_z^{mag}\}\end{aligned} \tag{21}$$

where $\mathbf{F}_M^{int}$ is the internal force that the carbon fiber tube applies to the finger, expressed in $\mathbb{W}$. $\mathbf{F}_M^{int}$ is calculated as:

$$\ddot{\mathbf{x}}_L = -\mathbf{R}_L\hat{\mathbf{\Omega}}_L^2\mathbf{L}_M + \mathbf{R}_L\hat{\mathbf{L}}_M\dot{\mathbf{\Omega}}_L \tag{22}$$

$$\ddot{\mathbf{x}}_1 = \mathbf{R}_L\hat{\mathbf{\Omega}}_L^2\mathbf{L}_{M1} - \mathbf{R}_L\hat{\mathbf{L}}_{M1}\dot{\mathbf{\Omega}}_L - \mathbf{R}_1\hat{\mathbf{\Omega}}_1^2\mathbf{d}_1 + \mathbf{R}_1\hat{\mathbf{d}}_1\dot{\mathbf{\Omega}}_1 \tag{23}$$

$$\ddot{\mathbf{x}}_2 = \mathbf{R}_L\hat{\mathbf{\Omega}}_L^2\mathbf{L}_{M2} - \mathbf{R}_L\hat{\mathbf{L}}_{M2}\dot{\mathbf{\Omega}}_L - \mathbf{R}_2\hat{\mathbf{\Omega}}_2^2\mathbf{d}_2 + \mathbf{R}_2\hat{\mathbf{d}}_2\dot{\mathbf{\Omega}}_2 \tag{24}$$

$$\mathbf{F}_1^{int} = m_1\ddot{\mathbf{x}}_1 - \mathbf{u}_1 + m_1 g\mathbf{e}_3 \tag{25}$$

$$\mathbf{F}_2^{int} = m_2\ddot{\mathbf{x}}_2 - \mathbf{u}_2 + m_2 g\mathbf{e}_3 \tag{26}$$

$$\mathbf{F}_M^{int} = -m_L\ddot{\mathbf{x}}_L - \mathbf{F}_1^{int} - \mathbf{F}_2^{int} - m_L g\mathbf{e}_3 \tag{27}$$

where $\mathbf{F}_i^{int}$ is the force that the link applies to each ARC-unit $i = 1, 2$ and $\dot{\mathbf{\Omega}}_1, \dot{\mathbf{\Omega}}_2, \dot{\mathbf{\Omega}}_L$ are derived from (15)-(18).

With respect to the reset maps $\mathscr{R}$, when the system switches from FF to AM mode, the point $\mathbf{x}_L$ will move on the surface of a sphere with the center at $\mathbf{x}_M = \mathbf{x}_{valve}$, thus the component of $\mathbf{v}_L$ that is parallel to $\mathbf{R}_L\mathbf{L}_M$ is zeroed. We also assume that the z-components of $\mathbf{\Omega}_L, \mathbf{\Omega}_M$ are small before and after the contact with the valve:

$$\mathbf{e}_{LM} = \frac{\mathbf{R}_L\mathbf{L}_M}{L_M} \tag{28}$$

$$\mathbf{v}_L^+ = \mathbf{v}_L - (\mathbf{v}_L\cdot\mathbf{e}_{LM})\mathbf{e}_{LM} \tag{29}$$

$$\mathbf{R}_L^T\mathbf{v}_L^+ = \mathbf{\Omega}_L^+ \times (-\mathbf{L}_M) \Rightarrow \mathbf{\Omega}_L^+ = -\hat{\mathbf{L}}_M\mathbf{R}_L^T\frac{\mathbf{v}_L^+}{L_M^2} \tag{30}$$

$$\mathscr{R}(FF, AM) = [\mathbf{R}_1, \mathbf{\Omega}_1, \mathbf{R}_2, \mathbf{\Omega}_2, \mathbf{R}_L, \mathbf{\Omega}_L^+, \mathbf{R}_{valve}, \mathbf{0}] \tag{31}$$

The reset map from AM to FF $\mathscr{R}(AM, FF)$ incorporates the constraints $\mathbf{x}_L = \mathbf{x}_M - \mathbf{R}_L\mathbf{L}_M, \dot{\mathbf{x}}_L = -\mathbf{R}_L\hat{\mathbf{\Omega}}_L\mathbf{L}_M$. Assuming that the damper between the link and the finger is stiff enough, then $\mathbf{R}_M \approx \mathbf{R}_L,\ \mathbf{\Omega}_M \approx \mathbf{\Omega}_L$ in FF. Thus:

$$\begin{aligned}\mathscr{R}(AM, FF) = [\mathbf{x}_M - \mathbf{R}_L\mathbf{L}_M, -\mathbf{R}_L\hat{\mathbf{\Omega}}_L\mathbf{L}_M, \mathbf{R}_1, \mathbf{\Omega}_1, \mathbf{R}_2, \mathbf{\Omega}_2, \\ \mathbf{R}_L, \mathbf{\Omega}_L, \mathbf{R}_L, \mathbf{\Omega}_L]\end{aligned} \tag{32}$$

V. CONTROL STRATEGY

In order to enable free-flight navigation and stable aerial manipulation, we develop respective controllers and use the following switching policies: the switch from FF to AM controller follows the guard map in (19) and the switch from AM to FF follows the guard map in (21) (activated by turning off the electromagnet). As can be seen from (10), (11), (15), (16), the rotational dynamics of the 2 ARC-units are independent of the translational and rotational dynamics of the link when we neglect the terms containing $\mathbf{d}_1, \mathbf{d}_2$. Thus, each ARC-unit can be thought of as a thrust vector individually controlled by its attitude controller. Assuming that the response of the attitude controller in each ARC-unit is much faster than the translational and rotational dynamics of the link, the reference thrust vector $\mathbf{u}_i^d$ $(i = 1, 2)$ for each ARC-unit can be tracked instantaneously. We derive the control law manipulating the thrust vector commands of the two ARC-units to guarantee the stability and tracking performance of ARC-M in both free-flight and aerial manipulation.

A. Controller for Free-flight Mode

The linearized model of the system around the hovering point in Free-flight mode is first derived. In order to decouple the x, y translational dynamics from the roll, pitch angular dynamics of the link, we will express the position of the link $(\mathbf{x}_L^\psi)$ and its reference position $(\mathbf{x}_L^{\psi,d})$ in the yaw-aligned $\mathbb{W}$:

$$\begin{aligned}\mathbf{x}_L^\psi &= \mathbf{R}_z^T(\psi_L)\mathbf{x}_L = (x_L^\psi, y_L^\psi, z_L) \\ \mathbf{x}_L^{\psi,d} &= \mathbf{R}_z^T(\psi_L)\mathbf{x}_L^d = (x_L^{\psi,d}, y_L^{\psi,d}, z_L^d) \\ \mathbf{e}_L^\psi &= \mathbf{R}_z^T(\psi_L)\mathbf{e}_L,\ \mathbf{e}_L = \mathbf{x}_L - \mathbf{x}_L^d\end{aligned} \tag{33}$$

We propose a parallel control architecture, shown in Fig. 4, consisting of four controllers for the link: the z controller, the yaw controller, the pitch and yaw-aligned $x_L(x_L^\psi)$ controller, as well as the roll and yaw-aligned $y_L(y_L^\psi)$ controller.

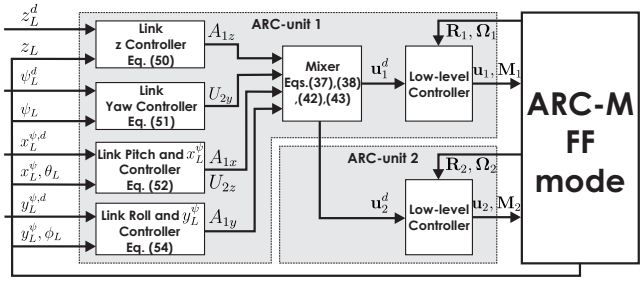

Fig. 4. ARC-M control diagram during the Free-flight mode.

Rewriting (9), (12), neglecting $\mathbf{d}_1, \mathbf{d}_2$'s terms, as:

$$(m_\Sigma)(\ddot{\mathbf{x}}_L + g\mathbf{e}_3) = \mathbf{u}_1 + \mathbf{u}_2 + m_M\mathbf{R}_L\hat{\mathbf{L}}_M\dot{\mathbf{\Omega}}_L - m_M\mathbf{R}_L\hat{\mathbf{\Omega}}_L^2\mathbf{L}_M \tag{34}$$

$$\begin{aligned}\mathbf{J}_{Lf}^*\dot{\mathbf{\Omega}}_L + \hat{\mathbf{\Omega}}_L\mathbf{J}_{Lf}^*\mathbf{\Omega}_L = \hat{\mathbf{L}}_1\mathbf{R}_L^T\mathbf{u}_1 + \hat{\mathbf{L}}_2\mathbf{R}_L^T\mathbf{u}_2 \\ - \hat{\mathbf{L}}_M\mathbf{R}_L^T\frac{m_M}{m_\Sigma}(\mathbf{u}_1 + \mathbf{u}_2) + \mathbf{M}_{fric}^L + \mathbf{M}_{twist}^L\end{aligned} \tag{35}$$

where $\mathbf{J}_{Lf}^* = \bar{J}_{Lf} + \frac{m_M^2}{m_\Sigma}\hat{\mathbf{L}}_M^2$. In Free-flight, assuming the damper is stiff enough to maintain $\mathbf{R}_L \approx \mathbf{R}_M$. We can sum (13) and (35) to obtain:

$$\mathbf{J}_{Lf}\dot{\mathbf{\Omega}}_L + \hat{\mathbf{\Omega}}_L\mathbf{J}_{Lf}\mathbf{\Omega}_L = \hat{\mathbf{L}}_1\mathbf{R}_L^T\mathbf{u}_1 + \hat{\mathbf{L}}_2\mathbf{R}_L^T\mathbf{u}_2 - \hat{\mathbf{L}}_M\mathbf{R}_L^T\frac{m_M}{m_\Sigma}(\mathbf{u}_1 + \mathbf{u}_2) \tag{36}$$

with $\mathbf{J}_{Lf} = \mathbf{J}_{Lf}^* + \mathbf{J}_M$. Let:

$$\mathbf{u}_1 = \frac{m_1}{m_1 + m_2}(m_\Sigma\mathbf{a}_1 + m_\Sigma g\mathbf{e}_3 + m_M\mathbf{R}_L\hat{\mathbf{\Omega}}_L^2\mathbf{L}_M) + \mathbf{u}_{rot2} \tag{37}$$

$$\mathbf{u}_2 = \frac{m_2}{m_1 + m_2}(m_\Sigma\mathbf{a}_1 + m_\Sigma g\mathbf{e}_3 + m_M\mathbf{R}_L\hat{\mathbf{\Omega}}_L^2\mathbf{L}_M) - \mathbf{u}_{rot2} \tag{38}$$

Plugging (37), (38) into (34), (36), we have:

$$m_\Sigma \ddot{\mathbf{x}}_L = m_\Sigma \mathbf{a}_1 + m_M \mathbf{R}_L \hat{\mathbf{L}}_M \dot{\boldsymbol{\Omega}}_L \tag{39}$$

$$\mathbf{J}_{Lf}\dot{\boldsymbol{\Omega}}_L + \hat{\boldsymbol{\Omega}}_L \left(\mathbf{J}_{Lf} - \frac{m_M^2}{m_\Sigma}\hat{\mathbf{L}}_M^2\right)\boldsymbol{\Omega}_L = \hat{\mathbf{L}}\mathbf{R}_L^T\mathbf{u}_{rot2} - \hat{\mathbf{L}}_M\mathbf{R}_L^T m_M(\mathbf{a}_1 + g\mathbf{e}_3) \tag{40}$$

Assuming $\ddot{\mathbf{x}}_L^d = \mathbf{0}$, we can rewrite (39) as:

$$\begin{aligned} m_\Sigma \ddot{\mathbf{e}}_L^\psi = {} & m_\Sigma \mathbf{R}_z(-\psi_L)\hat{\boldsymbol{\Omega}}_{Lz}^2 \mathbf{e}_L - m_\Sigma \mathbf{R}_z(-\psi_L)\hat{\boldsymbol{\Omega}}_{Lz}\mathbf{e}_L \\ & - 2m_\Sigma \mathbf{R}_z(-\psi_L)(\hat{\boldsymbol{\Omega}}_{Lz})\dot{\mathbf{e}}_L + m_\Sigma \mathbf{R}_y(\theta_L)\mathbf{R}_x(\phi_L)\mathbf{R}_L^T\mathbf{a}_1 \\ & + m_M \mathbf{R}_y(\theta_L)\mathbf{R}_x(\phi_L)\hat{\mathbf{L}}_M\dot{\boldsymbol{\Omega}}_L \end{aligned} \tag{41}$$

where $\boldsymbol{\Omega}_{Lz} = (0, 0, \Omega_{Lz})^T$ is the angular velocity of the link around z-axis in $\mathbb{B}_L$. We now derive the control law for the control inputs in $\mathbb{B}_L$ ($\mathbf{A}_1$ and $\mathbf{U}_2$):

$$\mathbf{R}_L^T\mathbf{a}_1 = \mathbf{A}_1 = (A_{1x}, A_{1y}, A_{1z})^T \Rightarrow \mathbf{a}_1 = \mathbf{R}_L\mathbf{A}_1 \tag{42}$$

$$\mathbf{R}_L^T\mathbf{u}_{rot2} = \mathbf{U}_2 = (0, U_{2y}, U_{2z})^T \Rightarrow \mathbf{u}_{rot2} = \mathbf{R}_L\mathbf{U}_2 \tag{43}$$

Assuming $\mathbf{J}_{Lf}$ is diagonal matrix (true when $\mathbf{J}_L, \mathbf{J}_M$ are diagonal matrices), let $\mathbf{J}_{Lf} = \mathbf{diag}(\mathbf{J}_{Lfx}, \mathbf{J}_{Lfy}, \mathbf{J}_{Lfz})$. Linearizing (40), (41) around the operating point $\mathbf{x}_L = \mathbf{x}_L^d, \dot{\mathbf{x}}_L = \dot{\mathbf{x}}_L^d (\mathbf{e}_L = \mathbf{e}_L^\psi = \mathbf{0}, \dot{\mathbf{e}}_L = \dot{\mathbf{e}}_L^\psi = \mathbf{0}), \phi_L = \theta_L = 0, \psi_L = \psi_L^d, \boldsymbol{\Omega}_L = \mathbf{0}, \mathbf{U}_2 = \mathbf{0}, \mathbf{A}_1 = \mathbf{0}$, we obtain:

$$m_\Sigma \ddot{e}_{Lx}^\psi = m_\Sigma A_{1x} + m_M L_M \dot{\Omega}_{Ly} \tag{44}$$

$$m_\Sigma \ddot{e}_{Ly}^\psi = m_\Sigma A_{1y} - m_M L_M \dot{\Omega}_{Lx} \tag{45}$$

$$m_\Sigma \ddot{e}_{Lz}^\psi = m_\Sigma A_{1z} \tag{46}$$

$$J_{Lfx}\dot{\Omega}_{Lx} = -m_M g L_M \phi_L - m_M L_M A_{1y} \tag{47}$$

$$J_{Lfy}\dot{\Omega}_{Ly} = -m_M g L_M \theta_L - L U_{2z} + m_M L_M A_{1x} \tag{48}$$

$$J_{Lfz}\dot{\Omega}_{Lz} = L U_{2y} \tag{49}$$

Assuming $\Omega_{Lz}^d = 0$ and $\dot{\Omega}_{Lz}^d = 0$, we choose the control law for $A_{1x}, A_{1z}, U_{2y}, U_{2z}$ as:

$$A_{1z} = -K_{pz}e_{Lz}^\psi - K_{dz}\dot{e}_{Lz}^\psi \tag{50}$$

$$U_{2y} = \frac{J_{Lfz}}{L}[-K_{p\psi}(\psi_L - \psi_L^d) - K_{d\psi}\Omega_{Lz}] \tag{51}$$

$$\begin{pmatrix} K_{11} & K_{12} \\ K_{21} & K_{22} \end{pmatrix}\begin{pmatrix} U_{2z} \\ A_{1x} \end{pmatrix} = \begin{pmatrix} H_1 \\ H_2 \end{pmatrix} \tag{52}$$

with

$$\begin{aligned} K_{11} &= -\frac{m_M L_M L}{J_{Lfy}}, K_{12} = m_\Sigma + \frac{m_M^2 L_M^2}{J_{Lfy}} \\ K_{21} &= -L, K_{22} = m_M L_M \\ H_1 &= m_\Sigma(-K_{px}e_{Lx}^\psi - K_{dx}\dot{e}_{Lx}^\psi) + \frac{m_M^2 L_M^2 g}{J_{Lfy}}\theta_L \\ H_2 &= J_{Lfy}(-K_{p\theta}\theta_L - K_{d\theta}\Omega_{Ly}) + m_M g L_M \theta_L \end{aligned}$$

From (45) and (47), we can derive the linear system governing $\mathbf{x}_{y\phi} = (e_{Ly}^\psi, \dot{e}_{Ly}^\psi, \phi_L, \Omega_{Lx})$ as:

$$\dot{\mathbf{x}}_{y\phi} = \underbrace{\begin{pmatrix} 0 & 1 & 0 & 0 \\ 0 & 0 & \frac{m_M^2 L_M^2 g}{m_\Sigma J_{Lfx}} & 0 \\ 0 & 0 & 0 & 1 \\ 0 & 0 & -\frac{m_M L_M g}{J_{Lfx}} & 0 \end{pmatrix}}_{\mathbf{A}_{y\phi}}\mathbf{x}_{y\phi} + \underbrace{\begin{pmatrix} 0 \\ 1 + \frac{m_M^2 L_M^2}{m_\Sigma J_{Lfx}} \\ 0 \\ -\frac{m_M L_M}{J_{Lfx}} \end{pmatrix}}_{\mathbf{B}_{y\phi}} A_{1y} \tag{53}$$

The dynamics in (53) are similar to the dynamics of the 2D cart-pendulum system. One can verify that this system is controllable, hence we can choose the control law

$$A_{1y} = -\mathbf{K}_{y\phi}\mathbf{x}_{y\phi} \tag{54}$$

based on pole-placement or LQR methods to stabilize the system. With the control law chosen in (50), (51), (52), (54), we can find the values of $\mathbf{a}_1, \mathbf{u}_{rot2}$ from (42) and (43) by substitution and derive the reference thrust vectors $\mathbf{u}_1^d, \mathbf{u}_2^d$ for the low-level attitude controllers by substituting $\mathbf{a}_1, \mathbf{u}_{rot2}$ into (37), (38).

We now prove the stability of the system in Free-flight mode. Rewriting the linear system described in (44)-(49) with the chosen control law, we obtain:

$$\ddot{e}_{Lx}^\psi = -K_{px}e_{Lx}^\psi - K_{dx}\dot{e}_{Lx}^\psi \tag{55}$$

$$\dot{\mathbf{x}}_{y\phi} = (\mathbf{A}_{y\phi} - \mathbf{B}_{y\phi}\mathbf{K}_{y\phi})\mathbf{x}_{y\phi} \tag{56}$$

$$\ddot{e}_{Lz}^\psi = -K_{pz}e_{Lz}^\psi - K_{dz}\dot{e}_{Lz}^\psi \tag{57}$$

$$\dot{\Omega}_{Ly} = -K_{p\theta}\theta_L - K_{d\theta}\Omega_{Ly} \tag{58}$$

$$\dot{\Omega}_{Lz} = -K_{p\psi}(\psi_L - \psi_L^d) - K_{d\psi}\Omega_{Lz} \tag{59}$$

where $(\mathbf{A}_{y\phi} - \mathbf{B}_{y\phi}\mathbf{K}_{y\phi})$ is a Hurwitz matrix. From the above equations, we can verify that $(\mathbf{e}_{Lx}^\psi, \mathbf{e}_{Ly}^\psi, \mathbf{e}_{Lz}^\psi, \dot{\mathbf{e}}_{Lx}^\psi, \dot{\mathbf{e}}_{Ly}^\psi, \dot{\mathbf{e}}_{Lz}^\psi, \phi_L, \Omega_{Lx}, \theta_L, \Omega_{Ly}, \psi_L - \psi_L^d, \Omega_{Lz})^T$ asymptotically converges to $\mathbf{0}$. Therefore, $\mathbf{x}_L = \mathbf{x}_L^d, \dot{\mathbf{x}}_L = \dot{\mathbf{x}}_L^d, \phi_L = \theta_L = 0, \psi_L = \psi_L^d, \boldsymbol{\Omega}_L = \mathbf{0}$ is the - desired - local asymptotically stable equilibrium point of the system in the Free-flight mode.

B. Controller for Aerial Manipulation Mode

In this mode, the thrust vectors of the two ARC-units are co-manipulated to control the angular dynamics of the link, as shown in Fig. 5. A nonlinear $\mathcal{SO}(3)$ angular controller [24] is utilized to calculate the necessary moments to control the angular dynamics of the link. A mixer commands the two ARC-units to generate the desired moments.

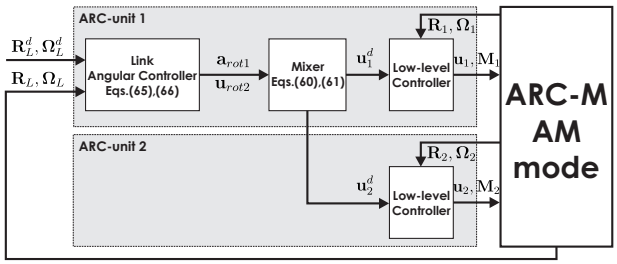

Fig. 5. ARC-M control diagram during Aerial Manipulation.

Rewriting (17), neglecting the terms containing $\mathbf{d}_1, \mathbf{d}_2$, with the transformation of control input:

$$\mathbf{u}_1 = m_1\mathbf{a}_{rot1} + \mathbf{u}_{rot2} + \frac{m_1}{m_1 + m_2}(m_1 + m_2 + m_L)g\mathbf{e}_3 \tag{60}$$

$$\mathbf{u}_2 = m_2\mathbf{a}_{rot1} - \mathbf{u}_{rot2} + \frac{m_2}{m_1 + m_2}(m_1 + m_2 + m_L)g\mathbf{e}_3 \tag{61}$$

we obtain:

$$\begin{aligned} \mathbf{J}_{La}\dot{\boldsymbol{\Omega}}_L = {} & \hat{\mathbf{L}}\mathbf{R}_L^T\mathbf{u}_{rot2} - \hat{\mathbf{L}}_M\mathbf{R}_L^T(m_1 + m_2)\mathbf{a}_{rot1} \\ & - \hat{\boldsymbol{\Omega}}_L\mathbf{J}_{La}\boldsymbol{\Omega}_L + \mathbf{M}_{fric}^L + \mathbf{M}_{twist}^L \end{aligned} \tag{62}$$

We now derive the control law for $\mathbf{a}_{rot1}, \mathbf{u}_{rot2}$ and calculate the reference thrust vectors $\mathbf{u}_1^d, \mathbf{u}_2^d$ for the two ARC-units from (60), (61) by substitution. Assuming that when the Aerial Manipulation mode is engaged, the desired angular rate and acceleration of the link are small:

$$\boldsymbol{\Omega}_L^d = \mathbf{0},\ \dot{\boldsymbol{\Omega}}_L^d = \mathbf{0} \tag{63}$$

The control law during aerial manipulation is chosen as:

$$\hat{\mathbf{L}}\mathbf{R}_L^T\mathbf{u}_{rot2} - \hat{\mathbf{L}}_M\mathbf{R}_L^T(m_1+m_2)\mathbf{a}_{rot1} = \underbrace{-k_{R_L}\mathbf{e}_{R_L} - k_{\Omega_L}\mathbf{e}_{\Omega_L} + \hat{\mathbf{\Omega}}_L\mathbf{J}_{La}\mathbf{\Omega}_L}_{\mathbf{M}_a} \tag{64}$$

where the attitude error vector $\mathbf{e}_{R_L}$ and the angular velocity error vector $\mathbf{e}_{\Omega_L}$ for the link are defined using (2), (3) as: $\mathbf{e}_{R_L} = \mathbf{e}_R(\mathbf{R}_L, \mathbf{R}_L^d), \mathbf{e}_{\Omega_L} = \mathbf{e}_\Omega(\mathbf{\Omega}_L, \mathbf{\Omega}_L^d)$. We assign:

$$\hat{\mathbf{L}}\mathbf{R}_L^T\mathbf{u}_{rot2} = L\hat{\mathbf{e}}_1\mathbf{R}_L^T\mathbf{u}_{rot2} = M_{az}\mathbf{e}_3 \overset{assign}{\rightarrow} \mathbf{u}_{rot2} = \frac{1}{L}\mathbf{R}_L M_{az}\mathbf{e}_2 \tag{65}$$

$$-\hat{\mathbf{L}}_M\mathbf{R}_L^T(m_1+m_2)\mathbf{a}_{rot1} = L_M\hat{\mathbf{e}}_3\mathbf{R}_L^T(m_1+m_2)\mathbf{a}_{rot1} = M_{ax}\mathbf{e}_1 + M_{ay}\mathbf{e}_2$$
$$\overset{assign}{\rightarrow} \mathbf{a}_{rot1} = \frac{1}{L_M(m_1+m_2)}\mathbf{R}_L(-M_{ax}\mathbf{e}_2 + M_{ay}\mathbf{e}_1) \tag{66}$$

By substituting $\mathbf{u}_{rot2}, \mathbf{a}_{rot1}$ as calculated in (65), (66) into (60), (61) we derive the desired control inputs $\mathbf{u}_1^d, \mathbf{u}_2^d$. The stability proof for the closed-loop system is given below. Assuming that the rotation angles between $\mathbf{R}_L, \mathbf{R}_M$ and $\mathbf{R}_L^d$ are strictly less than 180°, as per [27], there exists a positive number $\psi < 2$ such that:

$$\Psi(\mathbf{R}_L(t), \mathbf{R}_L^d(t)), \Psi(\mathbf{R}_L^d(t), \mathbf{R}_M(t)) \leqslant \psi < 2 \tag{67}$$

We also assume k_{R_L} is chosen such that:

$$k_{R_L} > 3\sqrt{2}B\lambda_M(\mathbf{k}_M),\ B = \sqrt{\frac{2}{2-\psi}} \tag{68}$$

We choose the Lyapunov function of the system as:

$$V_a = \frac{1}{2}\mathbf{e}_{\Omega_L}\cdot\mathbf{J}_{La}\mathbf{e}_{\Omega_L} + k_{R_L}\Psi(\mathbf{R}_L, \mathbf{R}_L^d) + c\mathbf{e}_R\cdot\mathbf{J}_{La}\mathbf{e}_\Omega + \frac{1}{2}\mathbf{\Omega}_M\cdot\mathbf{J}_{MC}\mathbf{\Omega}_M + \frac{1}{2}\mathbf{e}_R(\mathbf{R}_M, \mathbf{R}_L)\cdot\mathbf{k}_M\mathbf{e}_R(\mathbf{R}_M, \mathbf{R}_L) \tag{69}$$

where c is a positive constant satisfying:

$$c < \min\left\{\frac{\sqrt{k_{R_L}\lambda_m(\mathbf{J}_{La})}}{\lambda_M(\mathbf{J}_{La})}, \frac{4Ak_{\Omega_L}}{6\sqrt{2}A\lambda_M(\mathbf{J}_{La}) + k_{\Omega_L}^2}, \xi_1\right\} \tag{70}$$

, ξ_1 is the smaller positive root of the quadratic equation:

$$\epsilon Ak_{\Omega_L} - \left\{\epsilon\left[\frac{3\lambda_M(\mathbf{J}_{La})A}{\sqrt{2}} + \frac{k_{\Omega_L}^2}{4}\right] + \frac{\lambda_M(\mathbf{b}_M)k_{\Omega_L}}{4}\right\}\xi + \frac{3\lambda_M(\mathbf{J}_{La})\lambda_M(\mathbf{b}_M)}{4\sqrt{2}}\xi^2 = 0$$
$$, A = k_{R_L} - 3\sqrt{2}B\lambda_M(\mathbf{k}_M) > 0, \epsilon = \frac{\lambda_m(\mathbf{b}_M)}{\lambda_M(\mathbf{b}_M)} > 0$$

Plugging (64) into (62) and utilizing the assumption in (63), we obtain the AM-mode's closed-loop dynamics:

$$\mathbf{J}_{La}\dot{\mathbf{e}}_{\Omega_L} = -k_{R_L}\mathbf{e}_{R_L} - k_{\Omega_L}\mathbf{e}_{\Omega_L} + \mathbf{M}_{fric}^L + \mathbf{M}_{twist}^L \tag{71}$$

From the detailed report in [25], we have:

$$V_a \geqslant \mathbf{z}_1^T\mathbf{W}_1\mathbf{z}_1 + \frac{1}{2}\mathbf{\Omega}_M\cdot\mathbf{J}_{MC}\mathbf{\Omega}_M + \frac{1}{2}\mathbf{e}_R(\mathbf{R}_M, \mathbf{R}_L)\cdot\mathbf{k}_M\mathbf{e}_R(\mathbf{R}_M, \mathbf{R}_L) \tag{72}$$

$$\dot{V}_a \leqslant -\mathbf{z}_2^T\mathbf{W}_2\mathbf{z}_2 \tag{73}$$

$$\dot{V}_a = -ck_{R_L}||\mathbf{e}_{R_L}||_2^2 - k_{\Omega_L}||\mathbf{e}_{\Omega_L}||_2^2 + c\dot{\mathbf{e}}_R\cdot\mathbf{J}_{La}\mathbf{e}_\Omega - ck_{\Omega_L}\mathbf{e}_{R_L}\cdot\mathbf{e}_{\Omega_L} + c\mathbf{e}_{R_L}\cdot\left(\mathbf{M}_{fric}^L + \mathbf{M}_{twist}^L\right) - (\mathbf{R}_M\mathbf{\Omega}_M - \mathbf{R}_L\mathbf{\Omega}_L)\cdot\mathbf{b}_M(\mathbf{R}_M\mathbf{\Omega}_M - \mathbf{R}_L\mathbf{\Omega}_L) + \Omega_{Mz}M_{fric,z}^V \tag{74}$$

where $\mathbf{z}_1 = (||\mathbf{e}_{R_L}||_2, ||\mathbf{e}_{\Omega_L}||_2)^T \in \mathbb{R}^2$, $\mathbf{z}_2 = (||\mathbf{e}_{R_L}||_2, ||\mathbf{e}_{\Omega_L}||_2, ||\mathbf{R}_M\mathbf{\Omega}_M - \mathbf{R}_L\mathbf{\Omega}_L||_2)^T \in \mathbb{R}^3$ and the matrices $\mathbf{W}_1, \mathbf{W}_2$ are given by:

$$\mathbf{W}_1 = \frac{1}{2}\begin{pmatrix} k_{R_L} & -c\lambda_M(\mathbf{J}_{La}) \\ -c\lambda_M(\mathbf{J}_{La}) & \lambda_m(\mathbf{J}_{La}) \end{pmatrix} \tag{75}$$

$$\mathbf{W}_2 = \begin{pmatrix} cA & -\frac{c}{2}k_{\Omega_L} & -\frac{c}{2}\lambda_M(\mathbf{b}_M) \\ -\frac{c}{2}k_{\Omega_L} & k_{\Omega_L} - \frac{3}{\sqrt{2}}c\lambda_M(\mathbf{J}_{La}) & 0 \\ -\frac{c}{2}\lambda_M(\mathbf{b}_M) & 0 & \lambda_m(\mathbf{b}_M) \end{pmatrix} \tag{76}$$

With the condition in (68), (70), $\mathbf{W}_1$ and $\mathbf{W}_2$ are positive definite matrices. The Lyapunov function V_a is bounded from below and non-increasing, hence it converges to a limit [28]. Since $V_a(t) < V_a(0)$, then $||\mathbf{e}_{R_L}||_2, ||\mathbf{e}_{\Omega_L}||_2, ||\mathbf{\Omega}_M||_2, ||e_R(\mathbf{R}_M, \mathbf{R}_L)||_2$ are bounded. We also have from [24]:

$$||\dot{\mathbf{e}}_{R_L}||_2 \leqslant \frac{3}{\sqrt{2}}||\mathbf{e}_{\Omega_L}||_2$$

and since $||\mathbf{R}_L\mathbf{\Omega}_L - \mathbf{R}_M\mathbf{\Omega}_M||_2 \leqslant ||\mathbf{\Omega}_L||_2 + ||\mathbf{\Omega}_M||_2$, $||\dot{\mathbf{e}}_{R_L}||_2$ and $||\mathbf{R}_L\mathbf{\Omega}_L - \mathbf{R}_M\mathbf{\Omega}_M||_2$ are bounded. From (71), $||\dot{\mathbf{e}}_{\Omega_L}||_2$ is bounded, therefore $||\ddot{\mathbf{e}}_{R_L}||_2$ is also bounded. Assuming $||\mathbf{M}_{fric}^V||_2$ and $||\frac{d}{dt}\mathbf{M}_{fric}^V||_2$ are bounded, from (18), $\dot{\mathbf{\Omega}}_{Mz}$ is bounded and since $\mathbf{\Omega}_{Mx} = \mathbf{\Omega}_{My} = 0$ in the AM mode, then $||\dot{\mathbf{\Omega}}_M||_2$ is bounded. Differentiating the two sides of (74), we derive that $\ddot{V}_a$ is bounded. Per Barbalat's lemma [28], we have $\lim_{t\to\infty}\dot{V}_a = 0 \Rightarrow ||\mathbf{e}_{R_L}||_2, ||\mathbf{e}_{\Omega_L}||_2 \to 0$ as $t \to \infty$. From [25], we also have $||\mathbf{e}_R(\mathbf{R}_L^d, \mathbf{R}_M)||_2 \to 0$ as $t \to \infty$. As shown in [24], the only stable equilibrium of $\mathbf{R}_L, \mathbf{R}_M$ when $t \to \infty$ is $\mathbf{R}_L^d$.

Note: In terms of practical implementation, we choose k_{R_L}, k_{Ω_L} in (64) as diagonal matrices instead of scalar values as in [29]. The condition in (68) is conservative and corresponds to the specifically chosen Lyapunov function, therefore the elements of the matrix $\mathbf{k}_{R_L}$ are increased gradually until the system is stable in real experiments.

C. Stability Verification during Mode-switching

Beyond the individual controller stability for each of the FF and AM modes, we further study the stability during AM → FF and FF → AM switching. For the AM → FF case we limit our attention to the link's roll and yaw-aligned y dynamics which in practice will be most likely to deviate from the linearized model (ϕ_L can be large, while the desired roll angle is always 0). Assuming y-axis translation and rotation around the yaw-aligned x-axis we have:

$$\mathbf{\Omega}_L = [\Omega_{Lx}, 0, 0]^T = \Omega_{Lx}\mathbf{e}_1,\ \mathbf{e}_L^\psi = [0, e_{Ly}^\psi, 0]^T = e_{Ly}^\psi\mathbf{e}_2 \tag{77}$$

As detailed in [25] we derive the dynamics of ϕ_L and e_{Ly}^Ψ:

$$\begin{cases} \ddot{\mathbf{e}}_{Ly}^\psi &= \frac{m_M^2L_M^2g}{m_\Sigma J_{Lfx}}\cos\theta_L\tan\phi_L + \frac{1}{\cos\phi_L}\left(1 + \frac{m_M^2L_M^2}{m_\Sigma J_{Lfx}}\right)A_{1y} \\ \dot{\Omega}_{Lx} &= -\frac{m_ML_Mg}{J_{Lfx}}\cos\theta_L\sin\phi_L - \frac{m_ML_M}{J_{Lfx}}A_{1y} \end{cases} \tag{78}$$

where $-\pi/2 < \phi_L < \pi/2$. We perform reachability analysis with the CORA toolbox [30] to determine the set of initial states $[\phi_L^-, \Omega_{Lx}^-]$ in AM mode right before the switch to FF mode from which the closed-loop system with the control law A_{1y} chosen in (54) converges to the equilibrium point $\mathbf{0}$. The pitch angle of the link θ_L^- before the switch is set to 0 degrees

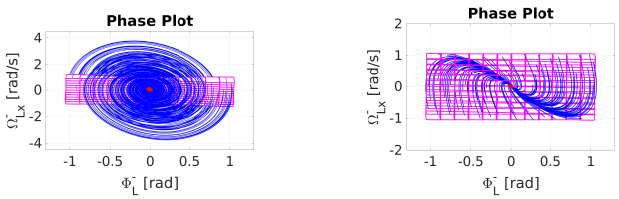

(a) AM → FF phase plot. (b) FF → AM phase plot.

Fig. 6. Phase plots from right before mode switch. Magenta rectangles: sets of initial states. Blue curves: trajectories from such sets of initial states. Red dot: equilibrium point $\mathbf{0}$.

for this study. The switching is implemented by following the reset function in (32).

For the FF → AM switching, the AM mode controller is nonlinear on $\mathcal{SO}(3)$ with the region of attraction as the region such that the rotation angles between $\mathbf{R}_L, \mathbf{R}_M$ and $\mathbf{R}_L^d$ are strictly less than 180 degrees and allows for stable behavior. We further verify the safety of the system in AM mode after the FF → AM switching by reachability analysis with the condition in (77), $\theta_L^- = \psi_L^- = 0$, and $\mathbf{R}_L^d = \mathbf{R}_M = \mathbf{R}_{valve} = \mathbf{I}_{3\times3}, \mathbf{\Omega}_L^d = \mathbf{\Omega}_M = \mathbf{0}_{3\times3}$, the phase plot is given in Fig. 6(b). To verify the system stability during FF → AM switching with a wide range of ϕ_L^-, we allow ϕ_L^- right before the switching to vary from $-\frac{\pi}{3}$ to $\frac{\pi}{3}$ although the guard in (19) requires that $\mathbf{R}_L \approx \mathbf{R}_M$ is close to $\mathbf{R}_{valve}$ for the FF → AM to occur. The switching is then implemented as per the reset function in (31).

D. ARC-M system with N ARC-units

The presented model may be extended to N ARC-units allowing the system to pickup multiple loads or increase the magnitude of exerted moments. By calculating the internal forces the link applies to neighbor ARC-units, the dynamics of an N ARC-unit system can be derived. This generalized ARC-M could be controlled using the proposed controller for the translation and angular dynamics of the first link (FF controller), or angular dynamics of the link corresponding to the contacted end-effector (AM controller), while the reference commands for the subsequent ARC-units can be derived using the parallel control architecture proposed in [12], with a time delay, ensuring that the internal forces are limited.

VI. EXPERIMENTAL STUDIES

A set of experimental studies were conducted using the ARC-M system to evaluate the stability and performance of its controller. The pose estimates of each ARC-unit and the connecting link are based on a Motion Capture system with sampling time $T_s = 0.02s$. In the first experiment, illustrated in Fig. 7, we demonstrate the ability of ARC-M to perform forceful work-task execution such as opening or closing an industrial valve. The ARC-M first operates in Free-flight mode to traverse to the location of the valve. The controller then switches to the Aerial Manipulation mode when the finger end-effector is attached to the valve by an electromagnet. The two ARC-units cooperate to exert a significant yaw moment (Fig. 7d) to rotate the valve by tilting around their roll axes, leveraging the length of the connecting link. The electromagnet is then turned off to detach the finger end-effector from the valve and the ARC-M switches back to Free-flight control to stabilize the roll and pitch angles of the link around zero as shown in Fig. 7c.

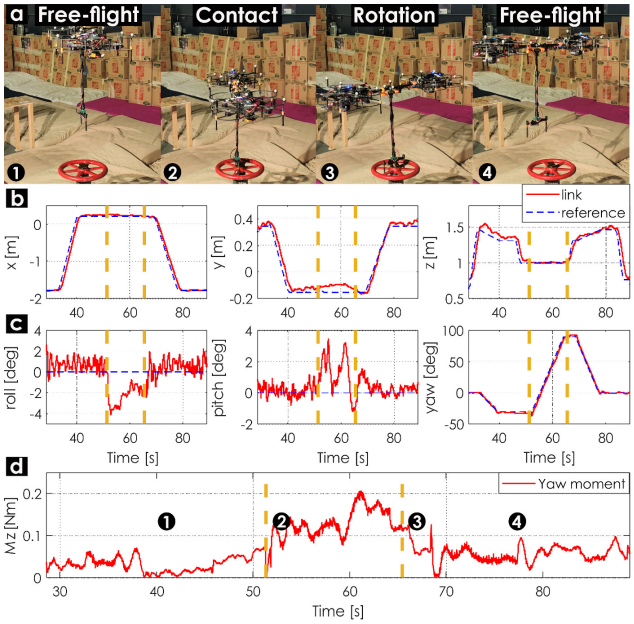

Fig. 7. Valve rotation experiment: a) sequence of ARC-M poses (1,4: Free-flight, 2,3: Aerial Manipulation), b) and c) position and angular tracking performance plots of the link, respectively, d) exerted yaw moment to the valve. Orange lines mark controller switching times.

The second experiment demonstrates the ability of the FF mode controller to suppress load oscillations. An additional load of 50g is attached to the finger. The ARC-M is commanded to hover at a fixed position. The slung load is then manually held at a nonzero roll angle and released. ARC-M reacts to this disturbance by moving in the yaw-aligned y axis as shown in Fig. 8a,b to stabilize the link's roll angle. Fig. 8c demonstrates that the system can be stabilizable for an initial link's roll of 40deg which is outside of the range of the small-angle assumption used to design the controller in Section V-A. We attribute this fact to a) the effect of gravity which will bring the finger to the downward vertical position and b) the small unmodelled friction between each ARC-unit and the link with the 3 DoF joints. The z axis spike in Fig. 8b is explained by the support of the human for the masses of the link and the end-effector (Fig. 8a1).

Finally, we also demonstrate the ARC-M in the context of pick-and-release tasks - here for a trash collection application. The ARC-M is able to stabilize the roll angle of the link after the pickup as illustrated in Fig. 9b. The offset in z axis observed in Fig. 9c after the pickup can be explained by the uncompensated mass of the trash.

VII. CONCLUSIONS

This paper presented the Aerial Robotic Chain Manipulator, its modeling and control. A hybrid dynamics model is derived consisting of Free-flight and Aerial Manipulation modes. Respective controllers for each mode are developed with stability guarantees. ARC-M and its controller are verified

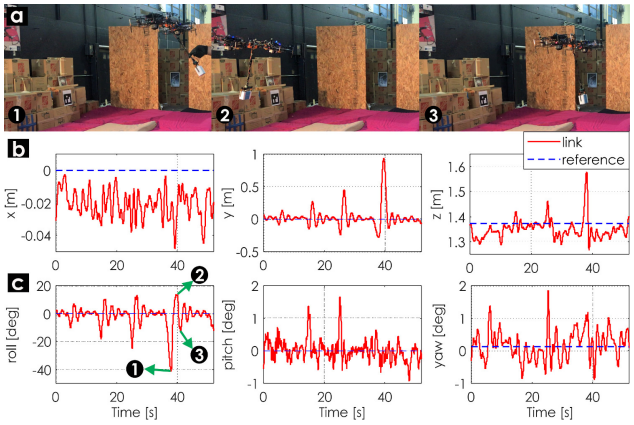

Fig. 8. Slung-load oscillation suppression: a) sequence of ARC-M poses when reacting to disturbances, b) and c) link position and angular tracking performance plots, respectively.

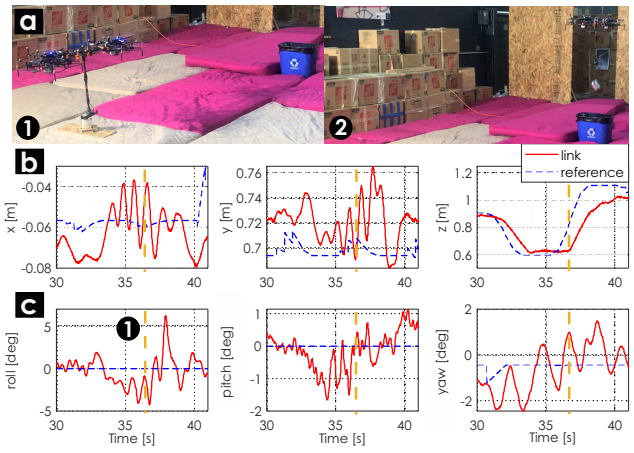

Fig. 9. Pick-and-release experiment: a) sequence of ARC-M poses, b) and c) position and angular tracking plots of the link, respectively. Orange line marks pickup time.

extensively in experimental studies including a forceful work-task of opening an industrial valve, evaluation of slung-load oscillation suppression and a pick-and-release scenario.

REFERENCES

[1] H. Yang and D. Lee, "Hierarchical cooperative control framework of multiple quadrotor-manipulator systems," in *2015 IEEE International Conference on Robotics and Automation (ICRA)*. IEEE, 2015.

[2] A. Suarez, G. Heredia, and A. Ollero, "Lightweight compliant arm for aerial manipulation," in *2015 IEEE/RSJ International Conference on Intelligent Robots and Systems (IROS)*. IEEE, 2015, pp. 1627–1632.

[3] H. B. Khamseh, F. Janabi-Sharifi, and A. Abdessameud, "Aerial manipulation—a literature survey," *Robotics and Autonomous Systems*, vol. 107, pp. 221–235, 2018.

[4] F. Ruggiero, V. Lippiello, and A. Ollero, "Aerial manipulation: A literature review," *IEEE Robotics and Automation Letters*, no. 3, 2018.

[5] M. Zhao, T. Anzai, F. Shi, X. Chen, K. Okada, and M. Inaba, "Design, modeling, and control of an aerial robot dragon: A dual-rotor-embedded multilink robot with the ability of multi-degree-of-freedom aerial transformation," *IEEE Robotics and Automation Letters*, 2018.

[6] M. Zhao, F. Shi, T. Anzai, K. Chaudhary, X. Chen, K. Okada, and M. Inaba, "Flight motion of passing through small opening by dragon: Transformable multilinked aerial robot," in *2018 IEEE/RSJ International Conference on Intelligent Robots and Systems (IROS)*. IEEE, 2018, pp. 4735–4742.

[7] H. Yang, S. Park, J. Lee, J. Ahn, D. Son, and D. Lee, "Lasdra: Large-size aerial skeleton system with distributed rotor actuation," in *2018 IEEE International Conference on Robotics and Automation (ICRA)*. IEEE, 2018, pp. 7017–7023.

[8] T. Anzai, M. Zhao, X. Chen, F. Shi, K. Kawasaki, K. Okada, and M. Inaba, "Multilinked multirotor with internal communication system for multiple objects transportation based on form optimization method," in *2017 IEEE/RSJ International Conference on Intelligent Robots and Systems (IROS)*. IEEE, 2017, pp. 5977–5984.

[9] M. Zhao, K. Kawasaki, K. Okada, and M. Inaba, "Transformable multirotor with two-dimensional multilinks: modeling, control, and motion planning for aerial transformation," *Advanced Robotics*, vol. 30.

[10] H.-N. Nguyen, S. Park, J. Park, and D. Lee, "A novel robotic platform for aerial manipulation using quadrotors as rotating thrust generators," *IEEE Transactions on Robotics*, vol. 34, no. 2, pp. 353–369, 2018.

[11] H.-N. Nguyen, S. Park, and D. Lee, "Aerial tool operation system using quadrotors as rotating thrust generators," in *2015 IEEE/RSJ International Conference on Intelligent Robots and Systems (IROS)*. IEEE, 2015, pp. 1285–1291.

[12] H. Nguyen, T. Dang, and K. Alexis, "The reconfigurable aerial robotic chain: Modeling and control," in *2020 IEEE International Conference on Robotics and Automation (ICRA)*. IEEE, 2020, pp. 5328–5334.

[13] G. Darivianakis, K. Alexis, M. Burri, and R. Siegwart, "Hybrid predictive control for aerial robotic physical interaction towards inspection operations," in *Robotics and Automation (ICRA), 2014 IEEE International Conference on*, May 2014, pp. 53–58.

[14] M. Fumagalli, R. Naldi, A. Macchelli, F. Forte, A. Q. Keemink, S. Stramigioli, R. Carloni, and L. Marconi, "Developing an aerial manipulator prototype: Physical interaction with the environment," *IEEE robotics & automation magazine*, vol. 21, no. 3, 2014.

[15] G. Gioioso, A. Franchi, G. Salvietti, S. Scheggi, and D. Prattichizzo, "The flying hand: A formation of uavs for cooperative aerial tele-manipulation," in *2014 IEEE International conference on robotics and automation (ICRA)*. IEEE, 2014, pp. 4335–4341.

[16] M. Kamel, K. Alexis, and R. Siegwart, "Design and modeling of dexterous aerial manipulator," in *2016 IEEE/RSJ International Conference on Intelligent Robots and Systems (IROS)*. IEEE, 2016.

[17] A. Gawel, M. Kamel, T. Novkovic, J. Widauer, D. Schindler, B. P. Von Altishofen, R. Siegwart, and J. Nieto, "Aerial picking and delivery of magnetic objects with mavs," in *2017 IEEE international conference on robotics and automation (ICRA)*. IEEE, 2017, pp. 5746–5752.

[18] M. Orsag, C. M. Korpela, S. Bogdan, and P. Y. Oh, "Hybrid adaptive control for aerial manipulation," *Journal of intelligent & robotic systems*, vol. 73, no. 1-4, pp. 693–707, 2014.

[19] S. Kim, S. Choi, and H. J. Kim, "Aerial manipulation using a quadrotor with a two dof robotic arm," in *2013 IEEE/RSJ International Conference on Intelligent Robots and Systems*. IEEE, 2013.

[20] V. Lippiello, J. Cacace, A. Santamaria-Navarro, J. Andrade-Cetto, M. A. Trujillo, Y. R. R. Esteves, and A. Viguria, "Hybrid visual servoing with hierarchical task composition for aerial manipulation," *IEEE Robotics and Automation Letters*, 2015.

[21] S. Park, J. Lee, J. Ahn, M. Kim, J. Her, G.-H. Yang, and D. Lee, "Odar: Aerial manipulation platform enabling omnidirectional wrench generation," *IEEE/ASME Transactions on mechatronics*, 2018.

[22] R. Goebel, R. G. Sanfelice, and A. R. Teel, *Hybrid Dynamical Systems: Modeling, Stability, and Robustness*. Princeton University Press, 2012. [Online]. Available: http://www.jstor.org/stable/j.ctt7s02z

[23] R. Sanfelice, D. Copp, and P. Nanez, "A toolbox for simulation of hybrid systems in matlab/simulink: Hybrid equations (hyeq) toolbox." New York, NY, USA: Association for Computing Machinery, 2013.

[24] T. Lee, "Robust adaptive attitude tracking on so(3) with an application to a quadrotor uav," *IEEE Transactions on Control Systems Technology*, vol. 21, no. 5, pp. 1924–1930, 2013.

[25] H. Nguyen, and K. Alexis, "The Aerial Robotic Chain - Manipulator: Appendix for Modeling and Control," available at https://tinyurl.com/ralARCM.

[26] T. Lee, "Computational geometric mechanics and control of rigid bodies," Ph.D. dissertation, University of Michigan, 2008.

[27] T. Lee, M. Leok, and N. H. McClamroch, "Geometric tracking control of a quadrotor uav on se (3)," in *49th IEEE conference on decision and control (CDC)*. IEEE, 2010, pp. 5420–5425.

[28] J. E. Slotine and W. Li, *Applied Nonlinear Control*. Prentice-Hall.

[29] D. Mellinger and V. Kumar, "Minimum snap trajectory generation and control for quadrotors," in *2011 IEEE International Conference on Robotics and Automation*, 2011, pp. 2520–2525.

[30] M. Althoff, "COntinuous Reachability Analyzer (CORA)." [Online]. Available: https://github.com/TUMcps/CORA